SANDIA REPORT
SAND2009-5964
Unlimited Release
Printed September 2009

Plasmonic devices and sensors built from ordered nanoporous materials

Mark D. Allendorf, Ronald J.T. Houk, Benjamin W. Jacobs, Farid El Gabaly, Noel N. Chang, A. Alec Talin, Dennis D. Graham, Stephen D. House, Ian M. Robertson, Yoji Kobayashi, Jeffery R. Long

Prepared by
Sandia National Laboratories
Albuquerque, New Mexico 87185 and Livermore, California 94550

Sandia is a multiprogram laboratory operated by Sandia Corporation,
a Lockheed Martin Company, for the United States Department of Energy's
National Nuclear Security Administration under Contract DE-AC04-94AL85000.

Issued by Sandia National Laboratories, operated for the United States Department of Energy by Sandia Corporation.

Available to DOE and DOE contractors from
U.S. Department of Energy
Office of Scientific and Technical Information
P.O. Box 62
Oak Ridge, TN 37831

Telephone: (865) 576-8401
Facsimile: (865) 576-5728
E-Mail: reports@adonis.osti.gov
Online ordering: http://www.osti.gov/bridge

Available to the public from
U.S. Department of Commerce
National Technical Information Service
5285 Port Royal Rd.
Springfield, VA 22161

Telephone: (800) 553-6847
Facsimile: (703) 605-6900
E-Mail: orders@ntis.fedworld.gov
Online order: http://www.ntis.gov/help/ordermethods.asp?loc=7-4-0#online

SAND2009-5964
Unlimited Release
Printed September 2009

Plasmonic devices and sensors built from ordered nanoporous materials

Ronald J.T. Houk[1], Benjamin W. Jacobs[1], Farid El Gabaly Marquez[1], Noel N. Chang[2], A. Alec Talin[3], Dennis D. Graham[4], Stephen D. House[4], Ian M. Robertson[4], Mark D. Allendorf[1], Yoji. Kobayashi,[5] Jeffrey R. Long[5]

[1]Sandia National Laboratories, Livermore, CA 94551-0969. [2]Department of Chemistry, University of Illinois Urbana-Champaign, 505 S. Matthews Ave. Urbana, IL 61801. [3]National Institute of Standards & Technology, 100 Bureau Dr. Gaithersburg, MD 20899. [4]Department of Materials Science and Engineering, University of Illinois Urbana-Champaign, 1304 W. Green St. Urbana, IL 61801. [5]Dept. of Chemistry, University of California, Berkeley.

Abstract

The objective of this project is to lay the foundation for using ordered nanoporous materials known as metal-organic frameworks (MOFs) to create devices and sensors whose properties are determined by the dimensions of the MOF lattice. Our hypothesis is that because of the very short (tens of angstroms) distances between pores within the unit cell of these materials, enhanced electro-optical properties will be obtained when the nanopores are infiltrated to create nanoclusters of metals and other materials. Synthetic methods used to produce metal nanoparticles in disordered templates or in solution typically lead to a distribution of particle sizes. In addition, creation of the smallest clusters, with sizes of a few to tens of atoms, remains very challenging. Nanoporous metal-organic frameworks (MOFs) are a promising solution to these problems, since their long-range crystalline order creates completely uniform pore sizes with potential for both steric and chemical stabilization. We report results of synthetic efforts. First, we describe a systematic investigation of silver nanocluster formation within MOFs using three representative MOF templates. The as-synthesized clusters are spectroscopically consistent with dimensions ≤ 1 nm, with a significant fraction existing as Ag_3 clusters, as shown by electron paramagnetic resonance. Importantly, we show conclusively that very rapid TEM-induced MOF degradation leads to agglomeration and stable, easily imaged particles, explaining prior reports of particles larger than MOF pores. These results solve an important riddle concerning MOF-based templates and suggest that heterostructures composed of highly uniform arrays of nanoparticles within MOFs are feasible. Second, a preliminary study of methods to incorporate fulleride (K_3C_{60}) guest molecules within MOF pores that will impart electrical conductivity is described.

ACKNOWLEDGMENTS

The authors would like to thank Drs. Raghunandan Bhakta and Nathan Ockwig for their technical assistance with various aspects of this project, Prof. Roya Maboudian and Dr. Nicola Ferralis of the University of California at Berkeley for initial XPS measurements, and Prof. Edward Solomon and David Heppner of Stanford University for their assistance with the EPR spectroscopy. This work was funded by the Sandia Laboratory Directed Research and Development program. The work at Illinois was supported by the U.S. Department of Energy under grant DE-FC36-05GO15064.

[Blank page following section.]

CONTENTS

FIGURES

TABLES

[Blank page following section.]

1. INTRODUCTION

The objective of this project is to lay the foundation for using ordered nanoporous materials known as metal-organic frameworks (MOFs) to create devices and sensors whose properties are determined by the dimensions of the MOF lattice. Our hypothesis is that because of the very short (tens of angstroms) distances between pores within the unit cell of these materials, enhanced electro-optical properties will be obtained. Specifically, we expect tunneling rates through MOFs will be greatly enhanced if a few unit cells can be deposited in a bridging fashion across patterned electrodes. In addition, our preliminary work shows that, unexpectedly, enhanced Raman signals are observed when MOF films are infiltrated with silver. Transmission electron microscopy (TEM) images show that the average size of the silver particles thus formed is smaller than the 5 nm typically thought be the lower limit for SERS to occur. These experiments also reveal that what appear to be silver nanowires passing through the nanopores of the lattice can sometimes form. Since nanoporous MOFs can have extremely high surface areas (more than a factor of 5 higher than the highest surface area zeolites) and have tailorable pore chemistry, the potential exists to create sensors that respond rapidly and specifically to analytes adsorbed within the pores. Alternatively, the dielectric (or potentially semiconducting) MOF could be used as the matrix for assembling highly ordered hybrid structures containing nanowires embedded in the the lattice. Interesting electrical properties may result if a paramagnetic MOF is used. Finally, MOFs could be used as removable templates, which could be dissolved chemically in the presence of protecting groups such as surfactants to allow the creation of either nanoparticles or nanowires with extremely narrow size distributions determined by the size of the MOF nanopores.

This project consisted of two efforts: 1) infiltration and characterization of MOFs with silver, using a novel liquid-phase technique to create silver nanoparticles and/or nanowires and 2) exploration of strategies for creating electrical conductivity within MOFs by doping with potentially conducting materials such as C_{60}, alkali metals, and polyaromatics such as anthracene. We showed that electron beams, such as those produced by electron microscopes, damage MOFs, causing the framework to collapse and allowing metal nanoclusters enclosed within the pores to agglomerate. In some cases, this degradation occurs extremely quickly (within seconds). As a result, the misleading impression is created that the nanoparticles originally created by infiltration are larger than the actual pores. It is now clear that MOFs are capable of stabilizing silver clusters as small as Ag_3 (determined by electron paramagnetic resonance; EPR) and that they can serve as effective templates for nanoparticles of the size of their pore dimensions.

[Blank page following section.]

2. SILVER CLUSTER FORMATION, DYNAMICS, AND CHEMISTRY IN METAL-ORGANIC FRAMEWORKS*

2.1 Introduction

Template-directed synthesis is a common route to a wide range of nanomaterials with well-defined shapes and sizes. Nanostructures with dimensions of tens to hundreds of nanometers can be straightforwardly realized with hard templates, such as anodic aluminum oxide (AAO). Even smaller dimensions can be achieved using soft templates, such as surfactants; however these templates do not provide a three-dimensional support structure and can make the particles inaccessible to the environment. Recently, MOFs have emerged as a promising new class of templates that combine the long-range order of hard templates with the small diameter and synthetically flexible environment of soft templates. In seminal work by the group of Fischer et al., both vapor-phase and solution methods were used to infiltrate MOFs with Pd, Pt, Au, Cu, and Ru (see refs. 1, 2 and references therein). Moon et al. also report the use of a redox-active MOF to create Ag and Au nanoparticles, although the generality of this method is limited because currently there are few redox-active MOFs.[3, 4] Our interest in MOF-templated metal particles stems from our recent demonstration that evaporating silver onto a MOF film produces an apparent surface-enhanced Raman scattering (SERS).[5] However, scanning electron microscopy (SEM) revealed no particles on the surface, suggesting that the MOF layer had been infiltrated by the silver.

Surprisingly, reported TEM analyses of metal@MOFs show metal clusters with dimensions several times larger than those of the MOF pores, typically 3 – 5 nm vs. 1.8 nm. The reasons for this are unclear, although in the case of Ag and Au particles the known high mobility of the metals is thought to be the cause.[6] When MOF-5 was used as the template, the MOF crystal apparently remained intact, even though the observed particles were much larger than the pores.[1, 2, 6, 7] Turner et al. reported that a focused TEM beam destroys the MOF-5 framework, but based on electron tomography concluded that 1 – 3 nm Ru and Pd clusters were formed inside the framework. However, they did not explain how particles larger than the pore could form without destroying the framework.[3, 4, 7] We initially hypothesized that MOFs with differing pore sizes, structures, and chemistries could serve as templates to create and stabilize silver nanoclusters, while also maintaining access to a solution or gas phase for SERS-based chemical sensing. The resulting systematic study described here demonstrates that both physical and chemical cluster templation occur in MOFs, confirming our hypothesis. In the process, however, we also discovered the likely answer to the larger-than-pore cluster phenomenon.

2.2 Experimental Methods

We chose three water-stable MOFs for this study, representing different canonical structures, to understand the effect of pore size and geometry on templated particles: Cu(BTC),[8] MOF-508,[9, 10] and MIL-68(In).[11] Cu(BTC) (also known as HKUST-1) has a primitive cubic structure with two types of individual spherical pores (~1.56 nm diameter for the accessible pore) based on Cu(II) and trimesic (benzenetricarboxylic) acid. MOF-508 is an interpenetrated, structurally flexible,

* This chapter has been accepted for publication in *Nano Letters*, Sept. 2009.

pillared-sheet structure with 1D-channels based on zinc, therephthalic (benzenedicarboxylic) acid and 4,4-bipyridine. MIL-68(In) is a Kagomé-type structure formed from indium and therephthalic acid and having open 1D-channels with 2.2 nm and 1.1 nm diameters. In all three cases the MOF secondary building unit contains metal-carboxylate linkages.

We infiltrated these MOFs using an aqueous-ethanolic solution of silver(I) nitrate. Solution-based infiltration of metal salts into MOFs has been demonstrated for Pd,[12] Ag,[13] and Au,[3, 4] but in these cases infiltration was accompanied by significant decomposition of the framework. Although our method precludes the use of IRMOFs due to their instability in aqueous environments,[14] it delivers silver efficiently to the pores of Cu(BTC), MOF-508, and MIL-68(In) without degradation, as shown by powder x-ray diffraction (PXRD; Fig. S1). Once within the pores the Ag(I) is reduced in the presence of EtOH to Ag(0) with essentially 100% yield (based on x-ray photoelectron spectroscopy; see below), as expected.[15]

Additional details may be found in Appendix A.

2.3 Results

Elemental analysis of the infiltrated products provides the first indication of the effects of pore geometry. Silver loadings of 8 w% in Cu(BTC), 29 w% in MOF-508, and 31 w% in MIL-68(In) were obtained. The reduced loading in Cu(BTC) reflects the relatively poor transport resulting from its small pore openings (~ 1 nm). Both MOF-508 and MIL-68(In) have channel-like pore structures that allow greater mobility of the Ag^+ ions through the MOF structure. The corresponding average per-pore loadings are 1.7, 3.2, and 19.3 Ag atoms for Cu(BTC), MOF-508, and MIL-68(In), respectively. Spectroscopic, TEM, and XRD evidence presented below indicate that Ag forms molecular-scale clusters distributed uniformly throughout the MOF crystals and that formation of particles larger than the pore dimensions occurs only at elevated temperatures or under electron-beam irradiation.

One would expect that TEM could provide clear evidence of infiltrated silver clusters, since under favorable circumstances even single atoms can be imaged, and contrast scales as the square of the atomic number.[16] Previous investigators reported that although the TEM beam damages the MOF framework this does not affect the size of the particles. Our investigation confirms the susceptibility of MOFs to TEM damage.[6, 7, 17] However, we reach a very different conclusion with respect to the templated clusters: namely, the TEM electron beam damages MOF structures so quickly (within a few seconds to at most 1 min) that it appears that metal-infiltrated samples are unchanged by the beam. We demonstrated this by performing TEM in bright-field mode. To minimize beam damage we used a small (50 μm) condenser lens aperture and maintained a defocused beam whenever possible to minimize the local beam current. We also cooled the MOF samples to ~100 K using a liquid nitrogen-cooled stage to further minimize beam damage.

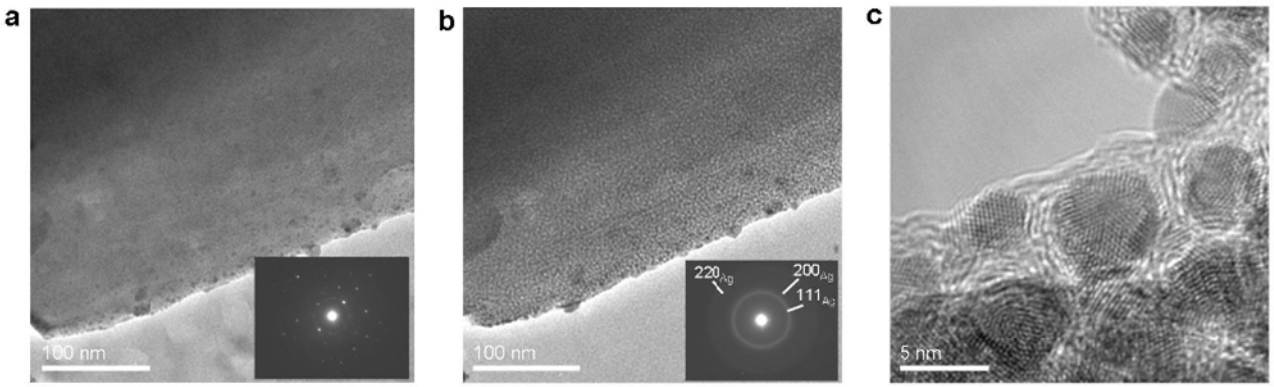

Figure 1. Before and after TEM images of Ag@MIL-68(In). a) TEM image of Ag@MIL-68(In) before significant electron beam damage. Inset is an SAED pattern of the MOF. B) TEM emage of Ag@MIL-68(In) after 1 minute exposure, showing significant beam damage. The inset is an SAED pattern of the MOF and coalesced Ag. C) HRTEM image of coalesced Ag particles.

The TEM images of Ag@MIL-68(In) in Figure 1 clearly illustrate these effects (data for the other two MOFs are provided in the Supporting Information). Upon illumination with the electron beam the MOF crystal structure begins to break down. The image of Ag@MIL-68(In) in Figure 1a was obtained after illumination for ~10 s. Already some beam degradation is observed, but the MOF crystal structure is still intact, as indicated by the selected area electron diffraction (SAED) pattern shown in the inset. The bright spots in the SAED pattern correspond to diffraction from the crystal structure of the MIL-68(In) sample. The larger dark-contrast particles seen in this image are Ag particles ~20 nm in diameter. The smaller dark-contrast areas within the MOF are Ag clusters that have just begun to coalesce. The image in Figure 1b was taken after the MOF sustained significant degradation by the electron beam. Here, the Ag has coalesced and grown into clusters with 2 – 5 nm diameters exhibiting clear lattice fringes (Fig. 1c). The SAED pattern in the inset of Fig. 1b corresponds to the cubic Ag crystal structure. Note that diffraction spots corresponding to the MOF crystal are no longer evident, indicating that the MOF crystal structure has been destroyed, while the polycrystalline Ag diffraction rings become clearly visible. The absence of distinguishable Ag diffraction rings prior to significant beam damage suggests that the Ag clusters are extremely small..

Video taken *in situ* in the TEM dramatically illustrates the MOF decomposition and subsequent Ag coalescence in real time (see Supporting Information).[4] The MOF crystal structure begins to break down almost immediately upon illumination with the electron beam. Waves of light and dark contrast can be seen, which indicate changing Bragg conditions in the MOF crystal structure. After the crystal structure has broken down, the infiltrated Ag begins to coalesce. This proceeds until clusters between 2 to 5 nm in diameter are formed, at which point the resulting structure becomes stable in the electron beam.

To provide even stronger evidence that Ag particles permeate the entire MOF template we performed electron tomography. Tomography is the process of reconstructing a three-

dimensional virtual object from individual images, which can then be transformed and manipulated to obtain images from a variety of viewing directions.[18, 19] Since the MOF template and Ag have significantly different average atomic mass, the contrast is sufficient to form useful images of Ag within the framework. A series of scanning transmission electron microscopy (STEM) images of the same area were collected for every degree of tilt over the range ±35° with a camera length of 15 cm. The images were aligned and the tomograph reconstructed; visualization of the reconstruction was then performed.[20, 21] A typical image is shown in Figure 2**,** from which it is evident that the Ag particles in the MOF are distributed throughout the framework. The Ag@MOFs are not 2-D objects and contain significant depth. An arbitrary cutoff for the contrast difference between framework and Ag does not affect the conclusion that the clusters are embedded regularly within the framework. Tomographic images were also obtained using a thin-tip stage that allows a much wider range of tilt angle (±70°) to reduce elongation effects in the reconstruction. These results are available in the Supporting Information.

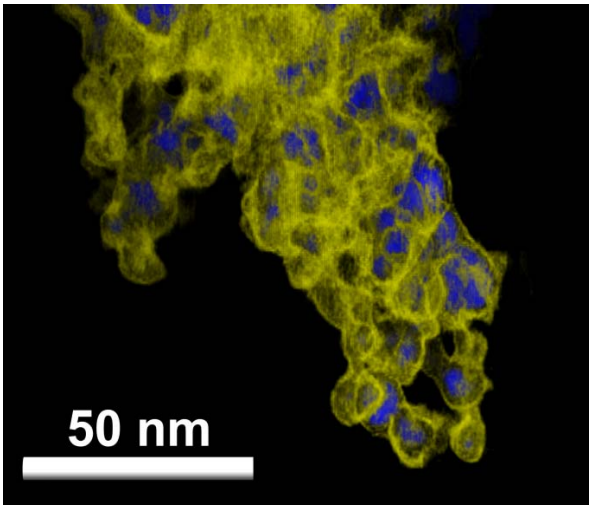

Figure 2. Three-dimensional tomographic reconstruction of Ag@MOF508, looking at part of a MOF crystal. Ag particles are dark (blue); the framework is light (yellow). The Ag particles are tightly intermixed throughout framework and not segregated at the surface.

In summary, our time-dependent TEM imagery, coupled with SAED diffraction patterns, indicate that as-synthesized Ag clusters in the MOF are much smaller than the particles revealed by extended exposure to the beam. SAED patterns, taken before significant electron beam damage to the MOF occurs, show that the MOF crystal structure remains intact after infiltration, as confirmed by the XRD measurements discussed above. Initially, the Ag clusters are too small to be readily imaged with a defocused TEM beam. High magnification, and consequently a focused electron beam, would be needed to resolve clusters on the scale of the MOF pores (1 – 2 nm). Since the MOF quickly breaks down under these conditions, it is virtually impossible to obtain images of the clusters in their as-infiltrated state. Only after the MOF breaks down and coalescence occurs can high-resolution images of Ag clusters be obtained. This explains the larger-than-pore clusters seen in other metal infiltrated MOFs. However, several questions still remain, such as the oxidation state of the as-synthesized Ag, the actual cluster size, and the types

of interactions with the MOF that keep the Ag from coalescing into larger particles, which we discuss below.

To determine the oxidation state of the Ag after infiltration, x-ray photoelectron spectroscopy (XPS) was performed (see Supporting Information.) The analysis confirms our expectation that using ethanol as the infiltration medium produces a reducing environment capable of forming Ag(0) *in situ.*[22] Reported binding energies for the Ag $3d^{5/2}$ peak range from 368.1 to 369.0 eV for neutral Ag, from 367.3 to 367.6 for Ag^{+}, and from 367.8 to 368.0 eV for Ag^{2+}.[23-27] XPS spectra for Ag@MOF[4] exhibit Ag $3d^{5/2}$ and $3d^{3/2}$ peaks at 368.6 and 374.6 eV, respectively, indicating that the Ag is uncharged. The escape depth of electrons at these energies is 20 – 30 Å, so XPS probes a depth of one or at most two MOF unit cells, so additional analytical techniques, sensitive to the bulk state of the material, are required to show that in our infiltrated MOF crystals Ag is distributed throughout the material.

Without the aid of electron-beam imaging techniques, the determination of actual size of the Ag clusters is not straightforward. Powder x-ray diffraction (PXRD) patterns of the as-synthesized Ag@MOF materials confirm that the long-range crystallinity of the MOF is unaffected by the infiltration process (Fig. S1.) Small changes in relative peak intensities are most likely the result of greater X-ray absorption by the infiltrated Ag, which perturbs the sharpness of the electron density function of the MOF unit cell.[2, 28] However, the PXRD patterns of all three Ag@MOFs exhibit no peaks attributable to crystalline (*fcc*) Ag. This result reinforces the conclusions that the particles have dimensions no larger than the MOF pores, since it is known that Ag clusters smaller than ~1 nm crystallize in icosahedral or decahedral geometry[29] and are too small to generate Bragg diffraction peaks.[30] There is also a slight possibility that the Ag is in an amorphous state; however, this is unlikely due the strong thermodynamic driving force towards crystallization.

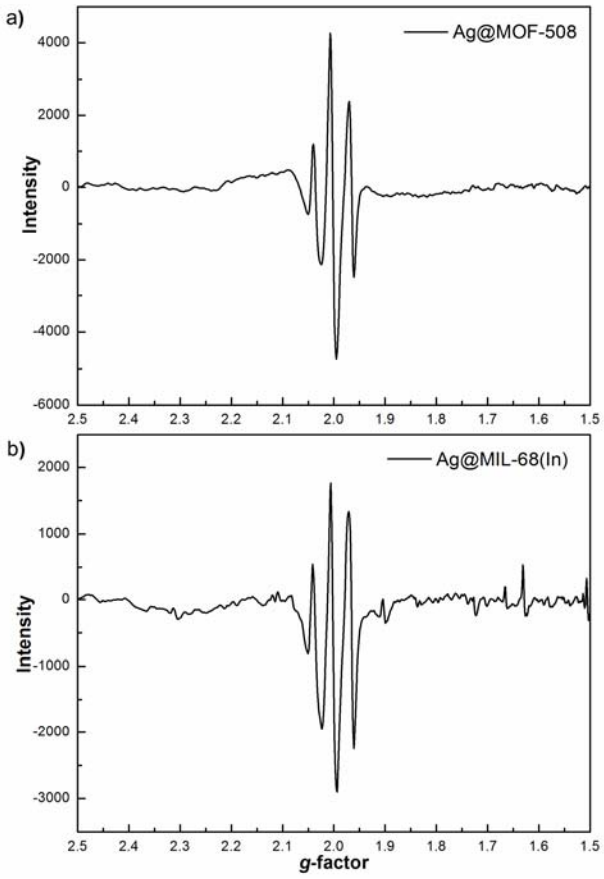

Figure 3. EPR spectra obtained at 77 K of a) Ag@MOF-508 and b) Ag@MIL-68(In) showing isotropic quartets centered at g = 2.002. These quartets are assigned to Ag_3^0 linear clusters.

Electron paramagnetic resonance (EPR) spectroscopy is sensitive to the bulk properties of a sample and has previously been used to show that small Ag clusters can be paramagnetic. EPR spectra of Ag@MOF-508 (3a) and Ag@MIL-68(In) (3b) exhibit a well-defined isotropic quartet centered at g = 2.001, which is expected for Ag(0).[3, 31] Unfortunately, this signal is obscured in Ag@Cu(BTC) by signals due to the triplet state of the binuclear Cu(II) building units and by a signal attributed to impurity mononuclear Cu(II) ions.[32] Previous work by Kevan et al. on small Ag clusters in zeolite templates assigns this isotropic quartet signal to linear Ag_3 clusters.[31] The strength of the signal indicates a significant population of the Ag_3^0 clusters throughout the bulk of the two templates, particularly in the Ag@MOF-508 material, where the pore size is small and the geometric barrier to coalescence is high.

To probe the mechanism behind the formation of these Ag_3 clusters, we endeavored to determine at which stage the Ag_3^0 species are formed. A previous report has claimed that Ag_3 clusters can spontaneously form in aqueous solutions, or that such species are inherently present as impurities in commercial $AgNO_3$ crystals.[33] In that report, mass spectrometry was employed to show that Ag_3 clusters exist within aqueous solutions and are the basis for the formation of triangular silver nanoplates. To test this theory, we performed ESI mass spectrometric studies on diluted samples

of our aqueous-ethanolic $AgNO_3$ precursor solutions (see Supporting Information.) Formation of Ag^0 clusters should be more favorable in our solvent mixture due to the reducing nature of ethanol. However no evidence of any Ag^0 cluster or adduct is observed. In fact, of the four species observed in the previous report, only one, $[Ag_3(NO_3)_2]^+$, was detected in our experiment (although several other $AgNO_3$ adducts are observed), indicating that all Ag in our solution prior to MOF infiltration exists as Ag^+. Moreover, the EPR spectrum of the undiluted $AgNO_3$ infiltration solution (see Supporting Information) shows only a very weak and unresolved signal This strengthens the conclusion that there is little to no Ag^0 present in solution prior to introduction into the MOF support.

Our results further indicate that the MOF provides both physical and chemical kinetic barriers to the Ag agglomeration. To assess the size of these barriers, differential scanning calorimetry (DSC) of infiltrated MOFs was performed and reveals Ag crystallization transitions between 250-310 °C (Fig. S3.) Interestingly, both MOF-508 and Cu(BTC) impart greater stability to the small particles with crystallization occurring at ~310 °C. MIL-68(In) with its larger pore diameters has a significantly lower transition temperature at ~250 °C. This result suggests that, while the infiltration of MIL-68(In) is the most efficient (19 Ag/pore), it is least able to stabilize small Ag clusters. PXRD patterns of Ag@MOF samples annealed at 300 °C show clear emergence of crystalline Ag reflections at 2θ = 38.1 corresponding to Ag(111) (Fig S2.) Analysis of these reflections using a Pearson type-VII curve fitting reveals an average particle size of ~15 nm based on the Debye-Scherer equation. Because the crystallization event is quite exothermic, as evidenced by DSC, it is likely that framework destruction and local coalescence is occurring during the annealing process. These observations are similar to the electron beam damage observed during TEM analysis in that Ag agglomeration occurs rapidly when the kinetic barrier to crystallization imposed by the MOF is overcome. The two methods are inherently different, however, in that annealing activates the Ag, whereas the electron beam destroys the MOF.

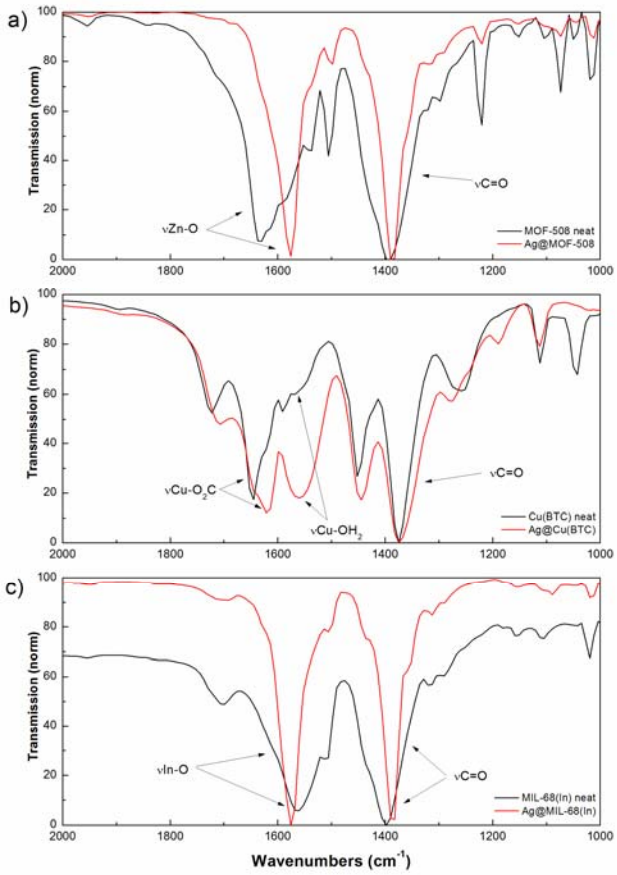

Figure 4. FTIR spectra of a) Ag@MOF-508 vs. neat MOF-508, b) Ag@Cu(BTC) vs. neat Cu(BTC), and c)Ag@MIL-68(In) vs. neat MIL-68(In). The percent transmission has been normalized.

The analyses above support the hypothesis that the MOFs are able to impose, at a minimum, steric constraints on the Ag clusters to maintain their small size. In addition, FTIR spectra show that MOFs provide chemical stabilization of clusters. The spectral changes induced by infiltration (Fig. 4) are evidence of the unique interactions between the clusters and each of the frameworks. In all three cases, the strong M-O (M = Cu, Zn, or In respectively) and C=O stretches are significantly perturbed, indicating that the Ag clusters interact with the majority of organic linker groups within the material. MOF-508 (Fig. 2a) shows a marked red-shift in the Zn-O stretch occurring at ~1640 cm^{-1}. The carbonyl stretch near 1390 cm^{-1} also shows a slight red-shift. The electron-rich carboxylate moiety of the secondary building unit (SBU) in MOF-508 should donate into a proximal silver cluster, weakening both the Zn-O and the C=O bonds. Cu(BTC) (Fig. 2b) shows somewhat different IR behavior upon silver infiltration. There are two different Cu-O stretches present in this MOF, one from the degenerate equatorial carboxylate bonds and one from axially coordinated water. In the neat material, the Cu-OH_2 mode at 1570 cm^{-1} is rather weak. However, the presence of a silver cluster near the SBU likely desymmetrizes this stretch *via* induction and bond distortion, leading to a red-shifted and much stronger absorbance. Note that the C=O stretch is largely unaffected, indicating that a greater interaction occurs between the silver and the water. This effect is also evidenced by the smaller red-shift of

the Cu-O_2C mode relative to the Zn-O shift in MOF-508. In MIL-68(In) (Fig. 2c), the In-O stretch is blue-shifted while the C=O stretch is again red-shifted. This phenomenon is likely due to the special case of indium being a row 5 and a main group element. The higher polarizability of indium with respect to zinc or copper allows electron donation to the silver cluster to occur through the indium preferentially to the carboxyl oxygen. This effect would lead to a strengthening of the In-O bond, which is highly coordinative. The strengthening of the In-O interaction comes at the price of weakening the carbonyl bond. In all cases, the presence of observable interactions in the IR supports the conclusion that the silver is both uniformly distributed, small, and chemically interactive with the MOF.

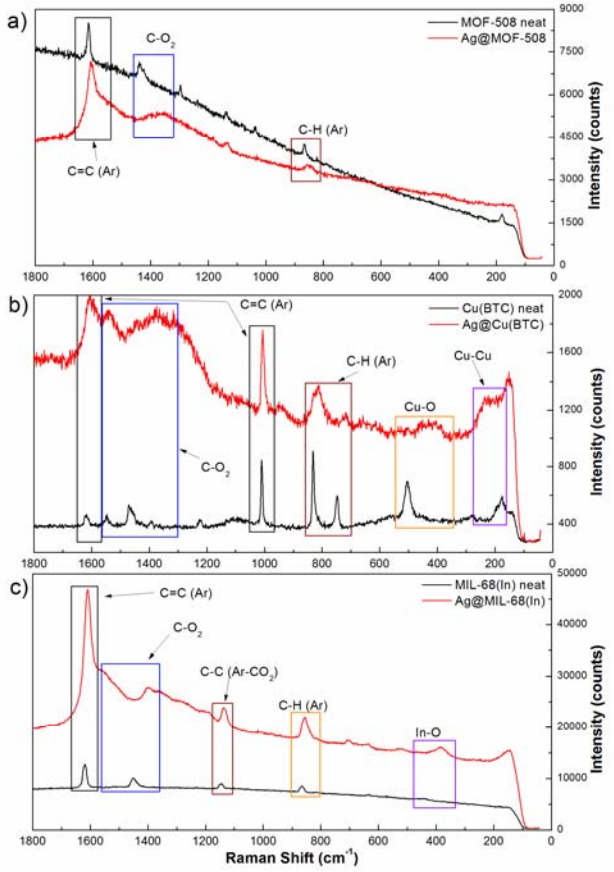

Figure 5. Raman spectra of Ag infiltrated vs. neat a) Cu(BTC), b) MOF-508, and c) MIL-68(In) showing increasing signal enhancement as the pore size increases from MOF-508<Cu(BTC)<MIL-68(In).

As mentioned above, we demonstrated that evaporating Ag onto Cu(BTC) apparently produces a SERS effect,[5] suggesting a particle-specific probe of the infiltrated MOFs described here. The Raman spectra of the three empty templates are compared with their Ag-infiltrated counterparts in Figure 5. MOF-508 (Fig. 5a), which at 6-7 Å has the smallest accessible pore, exhibits only minor changes in its Raman spectrum following infiltration, with a slight intensity enhancement of the ~1600 cm^{-1} breathing mode and the ~1390 cm^{-1} carboxylate symmetric stretch. As the pore size increases to 1.56 nm in Cu(BTC), a significant increase in the magnitude of the Raman

scattering perturbation occurs. The line shape seen in Figure 5b is identical to one we reported previously for evaporated Ag,[5] suggesting that both liquid-phase infiltration and metal evaporation produce similar MOF-cluster interactions. MIL-68(In), which has the largest and most accessible pores, exhibits the most strongly affected Raman spectrum compared to the empty framework. Observation of the In-O mode at ~400 cm^{-1} is particularly noteworthy because the metal cations in MIL-68 reside within a low-symmetry environment that typically reduces Raman intensities. This trend in the Raman enhancement appears to be correlated with the MOF pore size, providing additional evidence that the Ag clusters are restricted in their growth by the MOF. If the majority of Ag in these materials is in the form of Ag_3, it is unlikely that the changes observed in the Raman spectra are due to a plasmonic enhancement as previously postulated.[34] More likely the perturbations arise from local chemical interactions of the molecular-sized Ag clusters with the framework as was observed in the FTIR.

2.4 Conclusions

In conclusion, our investigation demonstrates that solution infiltration of three distinct MOFs with $AgNO_3$ results in uniform distribution of molecular Ag^0 clusters with sizes proportional to the MOF pore dimensions. EPR spectroscopy confirms the presence of paramagnetic clusters Ag_3 clusters. Vibrational spectroscopy supports the conclusion that the pore-included Ag clusters are both small in size (Raman spectroscopy) and well distributed throughout the MOF (FTIR). FTIR analysis also demonstrates the ability of the MOF to chemically constrain the agglomeration of Ag leading to a large kinetic barrier towards crystallization. Electron tomography confirms the hypothesis that the Ag is thoroughly dispersed throughout the template. Much larger particles observed by us and previous investigators using TEM are the result of damage to the MOF by the electron beam. Careful study of the effects of the TEM electron beam on these relatively soft materials shows that in our studies—and possibly in others—greater than pore-size clusters are largely artifacts of the imaging technique. Thus, care should be taken in the interpretation of electron microscopic data on MOFs and possibly other soft materials.

2.5 References

1. Hermes, S.; Schröder, F.; Amirjalayer, S.; Schmid, R.; Fischer, R. A. *J. Mater. Chem.* **2006,** 16, (25), 2464-2472.
2. Schröder, F.; Esken, D.; Cokoja, M.; van den Berg, M. W. E.; Lebedev, O. I.; Van Tendeloo, G.; Walaszek, B.; Buntkowsky, G.; Limbach, H.-H.; Chaudret, B.; Fischer, R. A. *J. Am. Chem. Soc.* **2008,** 130, (19), 6119-6130.
3. Moon, H. R.; Kim, J. H.; Suh, M. P. *Angew. Chem. Int. Ed.* **2005,** 44, (8), 1261-1265.
4. Suh, M. P.; Moon, H. R.; Lee, E. Y.; Jang, S. Y. *J. Am. Chem. Soc.* **2006,** 128, (14), 4710-4718.
5. Allendorf, M. D.; Houk, R. J. T.; Andruszkiewicz, L.; Talin, A. A.; Pikarsky, J.; Choudhury, A.; Gall, K. A.; Hesketh, P. J. *J. Am. Chem. Soc.* **2008,** 130, (44), 14404-14405.
6. Hermes, S.; Schröter, M.-K.; Schmid, R.; Khodeir, L.; Muhler, M.; Tissler, A.; Fischer, R. W.; Fischer, R. A. *Angew. Chem. Int. Ed.* **2005,** 44, (38), 6237-6241.
7. Turner, S.; Lebedev, O. I.; Schröder, F.; Esken, D.; Fischer, R. A.; Tendeloo, G. V. *Chem. Mater.* **2008,** 20, (17), 5622-5627.
8. Chui, S. S. Y.; Lo, S. M. F.; Charmant, J. P. H.; Orpen, A. G.; Williams, I. D. *Science* **1999,** 283, (5405), 1148-1150.
9. Chen, B.; Liang, C.; Yang, J.; Contreras, D. S.; Clancy, Y. L.; Lobkovsky, E. B.; Yaghi, O. M.; Dai, S. *Angew. Chem. Int. Ed.* **2006,** 45, (9), 1390-3.
10. Ma, B.-Q.; Mulfort, K. L.; Hupp, J. T. *Inorg. Chem.* **2005,** 44, (14), 4912-4914.
11. Volkringer, C.; Meddouri, M.; Loiseau, T.; Guillou, N.; Marrot, J.; Férey, G.; Haouas, M.; Taulelle, F.; Audebrand, N.; Latroche, M. *Inorg. Chem.* **2008,** 47, (24), 11892-11901.
12. Sabo, M.; Henschel, A.; Frode, H.; Klemm, E.; Kaskel, S. *J. Mater. Chem.* **2007,** 17, (36), 3827-3832.
13. Moon, H. R.; Kim, J. H.; Suh, M. P. *Angewandte Chemie-International Edition* **2005,** 44, (8), 1261-1265.
14. Greathouse, J. A.; Allendorf, M. D. *J. Am. Chem. Soc.* **2006,** 128, (33), 10678-10679.
15. Liz-Marzan, L. M.; Lado-Tourino, I. *Langmuir* **1996,** 12, (15), 3585-3589.
16. Pyrz, W. D.; Buttrey, D. J. *Langmuir* **2008,** 24, 11350.
17. Lebedev, O. I.; Millange, F.; Serre, C.; Van Tendeloo, G.; Férey, G. *Chem. Mater.* **2005,** 17, (26), 6525-6527.
18. Crowther, R. A.; Derosier, D. J.; Klug, A. *Proc. R. Soc. Lond., A* **1970,** 317, (1530), 40.
19. Hoppe, W.; Hegerl, R., Three-dimensional structure determination by electron microscopy (nonperiodic specimens). In *Computer processing of electron microscope images*, Hawkes, P. W., Ed. Springer-Verlag: Berlin, 1978; Vol. 13.
20. Harlow, M. L.; Ress, D.; Stoschek, A.; Marshall, R. M.; McMahan, U. J. *Nature* **2001,** 409, (6819), 484.
21. Pettersen, E. F.; Goddard, T. D.; Huang, C. C.; Couch, G. S.; Greenblatt, D. M.; Meng, E. C.; Ferrin, T. E. *J. Comput. Chem.* **2004,** 25, (13), 1605-1612.
22. Huang, Z. Y.; Mills, G.; Hajek, B. *J. Phys. Chem.* **1993,** 97, (44), 11542-11550.
23. Zemlyanov, D.; Weinberg, G.; Wild, U.; Schlögl, R. *Catal. Lett.* **2000,** 64, (2), 113-118.
24. Bao, X.; Muhler, M.; Schedel-Niedrig, T.; Schlögl, R. *Phys. Rev. B: Condens. Matter* **1996,** 54, (3), 2249-2262.

25. Moulder, J.; Stickle, W.; Sobol, P.; Bomben, K. *Chastain (Perkin-Elmer, Eden Prairie, MN, 1992)*, 118.
26. Morales, J.; Sanchez, L.; Martin, F.; Ramos-Barrado, J. R.; Sanchez, M. *J. Electrochem. Soc.* **2004,** 151, (1), A151-A157.
27. Lopez-Salido, I.; Lim, D.; Kim, Y. *Surf. Sci.* **2005,** 588, (1-3), 6-18.
28. Sauer, J.; Marlow, F.; Spliethoff, B.; Schuth, F. *Chem. Mater.* **2002,** 14, (1), 217-224.
29. Blom, M. N.; Schooss, D.; Stairs, J.; Kappes, M. M. *The Journal of Chemical Physics* **2006,** 124, (24), 244308.
30. Cullity, B.; Stock, S. *Reading: Addison-Wesley* **1967**.
31. Michalik, J.; Kevan, L. *J. Am. Chem. Soc.* **1986,** 108, (15), 4247-4253.
32. Poppl, A.; Kunz, S.; Himsl, D.; Hartmann, M. *J. Phys. Chem. C* **2008,** 112, (7), 2678-2684.
33. Xiong, Y.; Washio, I.; Chen, J.; Sadilek, M.; Xia, Y. *Angew. Chem. Int. Ed.* **2007,** 46, (26), 4917-4921.
34. Jiang, J.; Bosnick, K.; Maillard, M.; Brus, L. *J. Phys. Chem. B* **2003,** 107, 9964.

3. INFILTRATION OF MOFS WITH FULLERIDE

The similar size of some MOF pores and fullerenes (c. 1 nm) offers interesting possibilities by incorporating fullerenes and their alkali salt derivatives, fullerides, as guest species into the pores. Fullerides can be metallic or even superconducting, and these properties depend largely on the geometrical arrangement and spacing between the fulleride anions. Infiltrating the MOF pores with fullerides and using the pore structure of the MOF to control the fulleride arrangement should result in MOF-fullerene composites possessing interesting electronic properties. With partial loading of fullerenes into the pores, it may also be possible to preserve some porosity while still inducing electronic conductivity.

As a demonstration of the ability of fullerene C_{60} to infiltrate MOF pores, a previous report examines the solution-phase infiltration of neutral C_{60} (as opposed to fulleride) into the pores (11-12 Å) of MOF-177 (zinc benzene-1,3,5-tribenzoate).[1] Fullerides have also been incorporated via solution into one-dimensional pores of derivatized mesoporous silica.[2] In the latter case, the pore sizes are relatively large, and the fullerene molecules are expected to form disordered chains within the pores. Still, interesting electronic properties were observed.

For our work, we initially attempted to infiltrate MOFs with small, one-dimensional pores. We expected the smaller pores to force the fullerene molecules to form more ordered, 1-D chains which should show stronger interaction with each other, and hence more interesting electronic properties. Since the van der Waals diameter of C_{60} is known to be approximately 10.4 Å, MOFs with pore sizes within the range of 10-13 Å were chosen. The MOFs, shown below with their pore size diameters, are zinc 1,4-benzenedipyrazolate,[3] cobalt 2,5-dihyroxyterephalate (also known as CPO-27),[4] and copper [bis(4-carboxy-benzyl)]amine.[5]

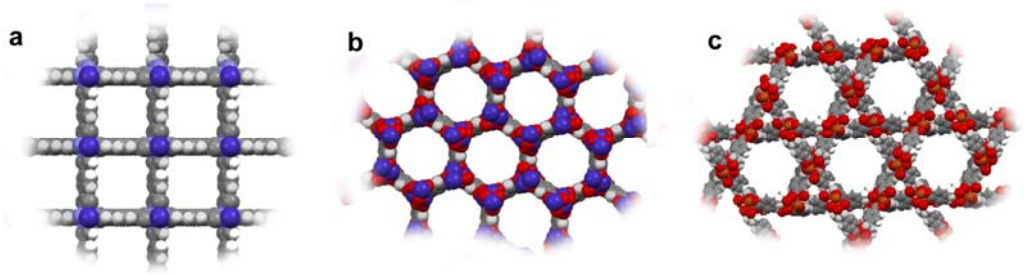

Figure 6. MOFs with 1-D pore structures: (**a**) zinc 1,4-benzenedipyrazolate (10 Å pores), (**b**) CPO-27 (11 Å pores), and (**c**) copper [bis(4-carboxy-benzyl)]amine (13 Å) pores.

We initially expected that the close size match between the pore and fullerene diameters would induce strong van der Waals interactions, which would serve as the driving force for the infiltration. Samples of the above MOFs were desolvated, and soaked in dry toluene solutions of C_{60} for periods up to weeks. However, based on the lack of color change in the otherwise white or light-colored MOFs and similar lack of color change in the supernatant, no significant amounts of C_{60} were incorporated into the pores with this method. Given the 1-D nature of the

pores, it is possible that the pores must be extensively desolvated, and it possible that solvent species or residual water may be enough to clog the pores.

Since it appears that the pore size of these 1-D pores may have been too small, or the 1-D nature is prone to clogging, we have also attempted to infiltrate the pores of MOF-177 with potassium fulleride (K_3C_{60}) in dry THF solution. This framework has been previously infiltrated with neutral C_{60} in toluene, although the structural integrity or infiltration yield has not been characterized. The smallest pore apertures are 10.8 Å, with larger chambers connected by these apertures. Powder samples of MOF-177 were desolvated, and then soaked in THF solutions of K_3C_{60} with approximately 0.7 pore volume equivalents of K_3C_{60}. After soaking for 2 weeks, the MOF sample was washed and filtered. Visual analysis, combined with powder XRD, shows that a heterogeneous mixture of fullerene/fulleride and MOF, together with a loss of crystallinity in the MOF has resulted. The disordered MOF results even pristine MOF samples are soaked in dry THF with no fulleride. Hence, it may be caused by the solvent or during other steps, rather than action of the fulleride. We are currently investigating the use of alternative solvents for the infiltration of K_3C_{60} into the pores of MOF-177.

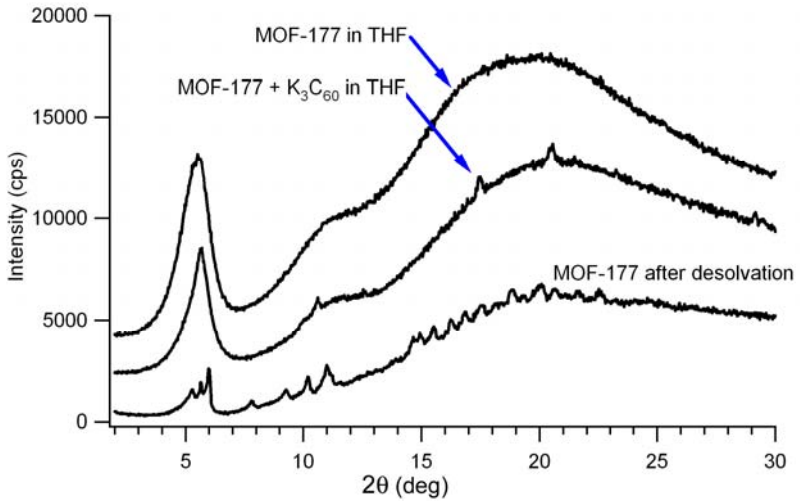

Figure 7. XRD patterns showing loss of crystallinity of desolvated MOF-177 upon soaking in THF and K_3C_{60}/THF. The small new peaks in the K_3C_{60}/THF-treated sample indicate that a cubic fullerene/fulleride phase has formed.

1. Chae, H. K.; Siberio-Perez, D. Y.; Kim, J.; Go, Y.; Eddaoudi, M.; Matzger, A. J.; O'Keeffe, M.; Yaghi, O. M. *Nature* **2004**, *427*, 523-527.
2. B. Ye; Trudeau, M. L.; Antonelli, D. M. *Adv. Mater.* **2001**, *13*, 561-565.
3. Choi, H. J.; Dinca, M.; Long, J. R. *J. Am. Chem. Soc.* **2008**, *130*, 7848-7850.
4. Pascal D. C. Dietzel; Morita, Y.; Blom, R.; Fjellvåg, H. *Angew. Chem. Int. Ed.* **2005**, *44*, 6354-6358.
5. Horike, S.; Hasegawa, S.; Tanaka, D.; Higuchi, M.; Kitagawa, S. *Chem. Commun.* **2008**, 4436.

[Blank page following section.]

APPENDIX A. SUPPORTING INFORMATION

General

All reagents were purchased from Aldrich or Acros, and solvents were purchased from Fisher and used without purification. FTIR was performed in solid state as KBr pellets on a BioRad FTS-40 infrared spectrophotometer. Powder X-ray diffraction was conducted on a Scintag XDS 2000 with 45 kV 40 mA Cu kα x-ray source using dual 1mm soller slits for source and dual 0.5 mm slits for the detector. MOF samples were typically scanned at 0.03º/step and 1.5 sec dwell time. Raman spectra were collected on an Acton SpectraPro model 2750 0.75 m triple spectrometer, with a Spectra Physics diode pumped and frequency doubled Nd:YAG 532 nm laser as the excitation source at a power of ~0.25 mW at the sample. All spectra were taken with a microprobe apparatus consisting of a 20× objective to focus the incident light to a spot of ~2 μm2 and collect the scattered light in 180° backscattering geometry. Samples were exposed from 2-30 seconds depending on the strength of the signal.

MOF Synthesis

Cu(BTC): Copper(II) nitrate trihydrate (2.9 g, 3 eq.) is dissolved in 25 mL of nanopure water. Trimesic acid (1.68 g, 2 eq.) is dissolved separately in 25 mL of 200 proof ethanol. The solutions are mixed in a pyrex media jar and capped tightly. The reaction vessel is sealed in a thick-walled PTFE jar for secondary containment, and the apparatus is placed in an oven at 110 °C for 24 hours. The blue crystalline precipitate is filtered and washed 3x with ethanol then 3x with water and allowed to air dry for 3 days. The reaction gives a yield of 75% based on copper. The crystals are activated under low vacuum (10^{-1} Torr) at 180 °C over night. Note that re-exposure to ambient atmosphere will hydrate the open coordination sites on the copper building units. The powder x-ray diffraction pattern is consistent with the literature. [1] Activated Cu(BTC) was found to have a Langmuir surface area of 1352 m^2/g .

MOF-508: Zinc(II) nitrate hexahydrate (703 mg, 1 eq.), terephthalic acid (393 mg, 1 eq.), and 4,4′-dipyridyl (185 mg, 0.5 eq.) are dissolved in 200 mL of 1:1 ethanol/DMF in a pyrex media jar. The jar is capped tightly and placed in a 90 °C oven for 24 hours. Upon completion, the white crystalline powder is filtered and washed with 3 x 30 mL DMF then 2 x 30 mL hexanes. The yield as synthesized based on zinc is 82%. The framework is activated under low vacuum (10^{-1} Torr) at 180 °C overnight. Both the as synthesized and activated powder x-ray diffraction patterns are consistent with the literature.[2] Activated MOF-508 was found to have a Langmuir surface area of 592 m^2/g.

MIL-68(In): Indium(III) nitrate (2.45 g, 1 eq.) and terephthalic acid (1.2 g, 1.15 eq.) are dissolved in 30 mL DMF in a pyrex media jar with sonication and heating. The reaction vessel is tightly capped and placed in an oven at 100 °C for 2 days. The MOF precipitates in large (200 μm) crystallites, which are allowed to cool and are then filtered and washed with DMF. Yield based on Indium is 80%. The MOF is activated under low vacuum (10^{-1} Torr) at 180 °C over night and gives an x-ray powder diffraction pattern consistent with the literature.[3] Activated MIL-68(In) was found to have a Langmuir surface area of 956 m^2/g.

Ag Infiltration

In a typical infiltration experiment, ~100 mg of the chosen MOF was activated under low vacuum (10^{-1} Torr) at 180 °C for 16 hours, then further evacuated at room temperature on a schlenk apparatus (10^{-2} Torr.) Ag(I) nitrate (256 mg, 1.5 mmol) was dissolved in 500 µL nanopure water then diluted to 3 mL with 200-proof ethanol to generate a 0.5 M $AgNO_3$ solution in 5:1 ethanol/water. The Ag salt solution was then cannulated into a glass vial containing the evacuated MOF to generate a slurry. The reaction vessel was backfilled with N_2, sonicated for 2 minutes to ensure thorough mixing, placed on a shaker and agitated 16 hours at 250 rpm. Following thorough washing to remove excess salt or unbound Ag particles, the samples were reactivated at 200 °C and 10^{-1} Torr for 16 hours.

Powder x-ray diffraction

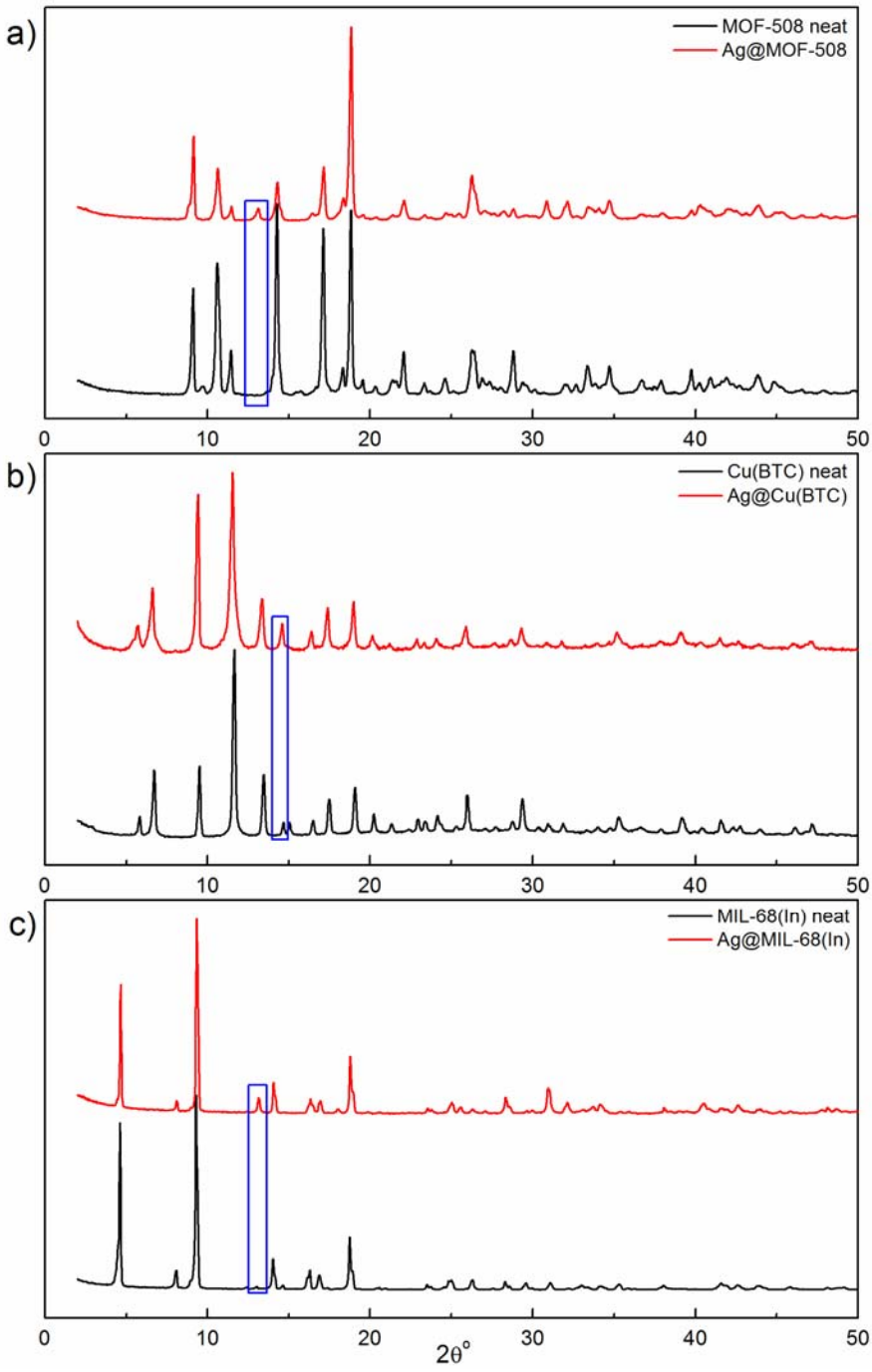

Figure S1. Powder x-ray diffraction patterns of a) MOF-508, b) Cu(BTC), and c) MIL-68(In) before and after Ag infiltration. The blue boxes indicate reflections of the framework which show dramatic relative intensity shifts due to x-ray absorption by nearby Ag clusters such that they almost appear to be new reflections.

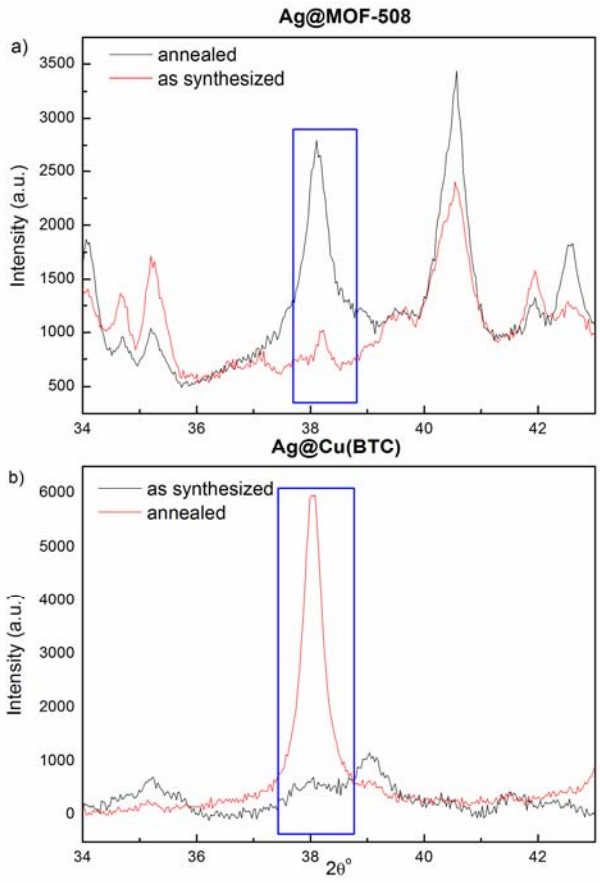

Figure S2: Powder X-ray diffraction patterns of a) Ag@MOF-508 and b) Ag@Cu(BTC) before and after annealing at 300 °C (10 min). The blue box indicates the Ag(111) reflection centered at 2θ = 38.1°. MIL-68(In) shows background reflections from the MOF which prevent observation of the Ag.

Differential Scanning Calorimetry

Differential scanning calorimetry was conducted on a Mettler-Toledo DSC822 at a ramp rate of 10 °/min under a 20 mL/min Ar flow. For MOF-508 and MIL-68(In) samples the temperature range was 25-475 °C and Cu(BTC) samples were run from 25-400 °C

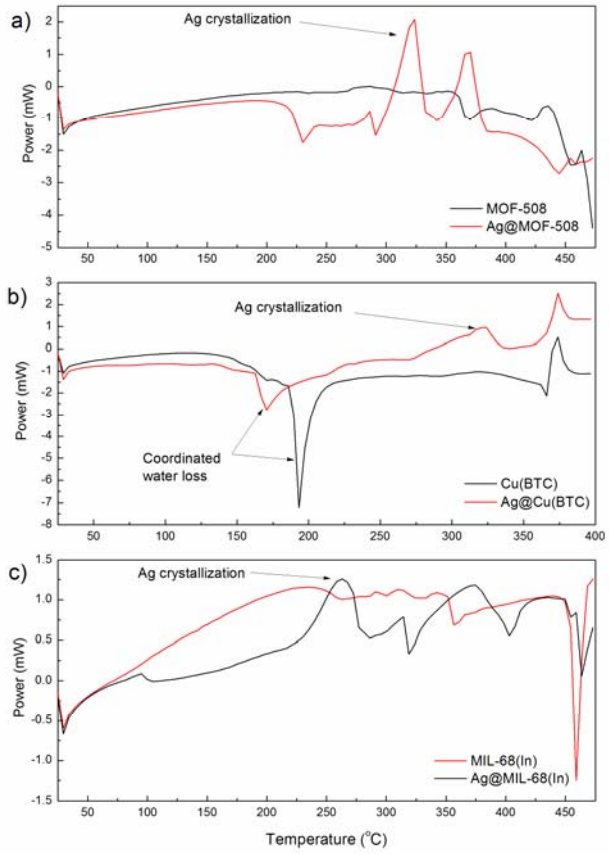

Figure S3. DSC traces of a) MOF-508, b) Cu(BTC) and c) MIL-68(In) before and after Ag-infiltration. Ag@MOF-508 shows two large exothermic peaks at 312 and 370 °C. Based on the annealing experiments, the transition at 312 °C is determined to be the initial Ag-crystallization while the higher temperature transition is likely a framework reorganization, consistent with TGA data.[1] Ag@Cu(BTC) shows the crystallization transition again around 315 °C. The DSC confirms the hypothesis that Ag weakens the axial water coordination at the Cu building units allowing the release of those waters at lower temperature. Ag@MIL-68(In) shows a much lower temperature crystallization transition than the other two materials. Likely, this is due to the larger pore spaces allowing more physical mobility of the Ag clusters.

X-ray Photoelectron Spectroscopy

XPS analysis was conducted with a HAC 5000 (VSW) spectrometer and a DAR 400 (Omicron) Al Kα (1486.6 eV) X-ray radiation source. The chamber pressure was below 1×10^{-8} Torr during the data acquisition. The binding energies were calibrated using the peak position of hydrocarbon (C1s) at 284.8eV.

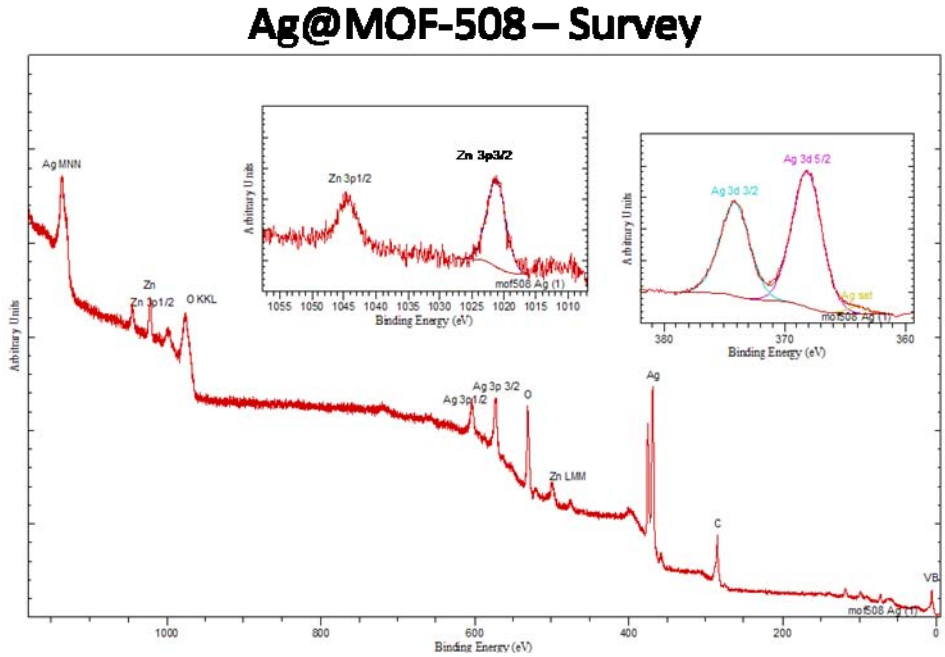

Figure S4. XPS survey of Ag@MOF-508 taken on a film drop cast from ethanol on ALD-aluminum oxide on silicon. The insets show regions corresponding to the Zn 3p and Ag 3d electrons. The insulating alumina surface causes the sample to charge, inducing a shift to higher energy of ~3.8 eV.

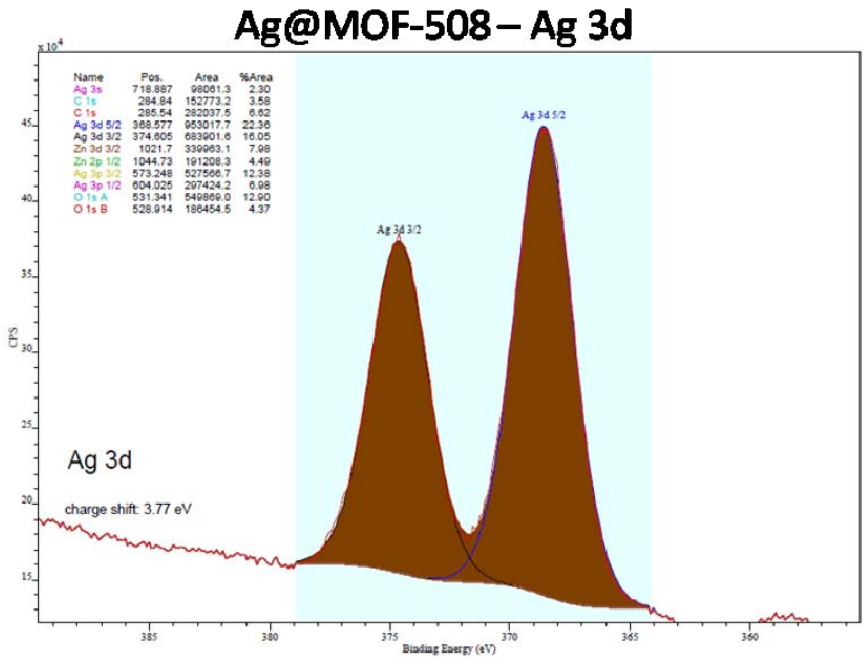

Figure S5. XPS of Ag@MOF-508 in the Ag(0) with the Ag $3d^{5/2}$ and Ag $3d^{3/2}$ highlighted and fit to Gaussian-Lorentzian functions. Each peak is well resolved, singular, and corresponds to binding energies of 368.6 and 374.6 eV, respectively, after reference to the standard C 1s and accounting for charging.

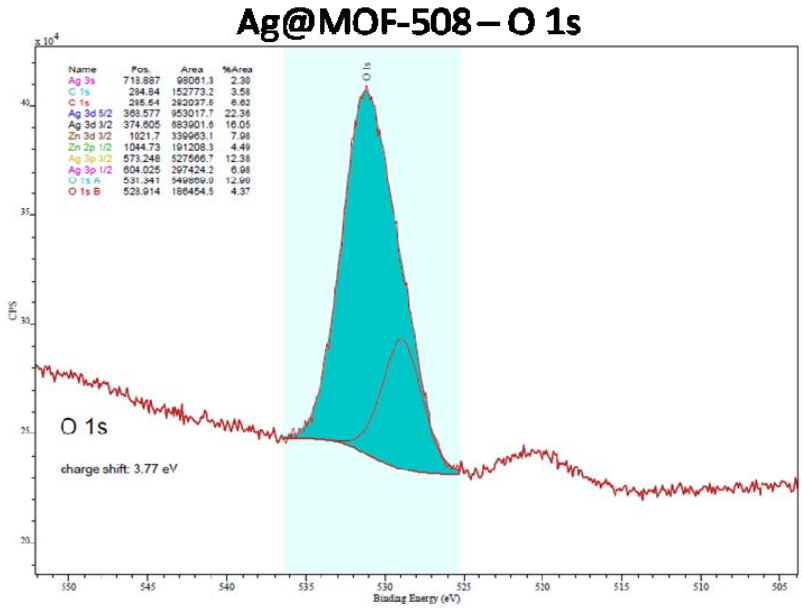

Figure S6. XPS of Ag@MOF-508 on alumina@silicon showing the O 1s region corrected for charging. Here the Gaussian-Lorentz fitting reveals two contributions to the overall signal. The small lower energy shoulder centered at 528.9 eV corresponds to the alumina support. The main peak centered at 531.3 eV arises from the MOF sample. This data shows well the effect of charging on the MOF due to x-ray absorption on the insulating surface.

Electron Paramagnetic Resonance

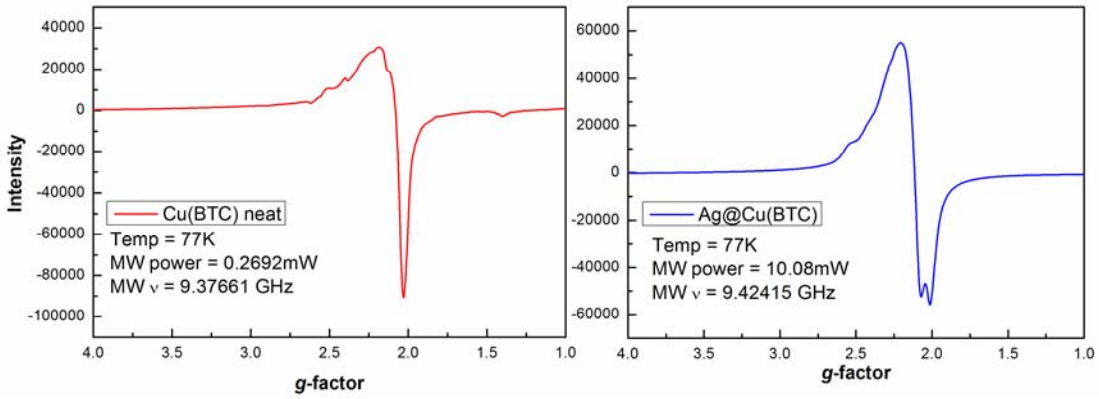

Figure S7. EPR spectra of Cu(BTC) (left) and Ag@Cu(BTC) (right) taken at 77K. In both cases, the signal is dominated by the characteristic $Cu(OAc_2)$ dimer from the SBU of the Cu(BTC) framework. The spectrum of the neat MOF was taken at low power to help improve the resolution of the dimer spin state. The appearance of a poorly resolved peak at g = ~2 in the Ag@Cu(BTC) may be caused by the presence of Ag_3 clusters; however without full resolution, this conclusion is only speculative.

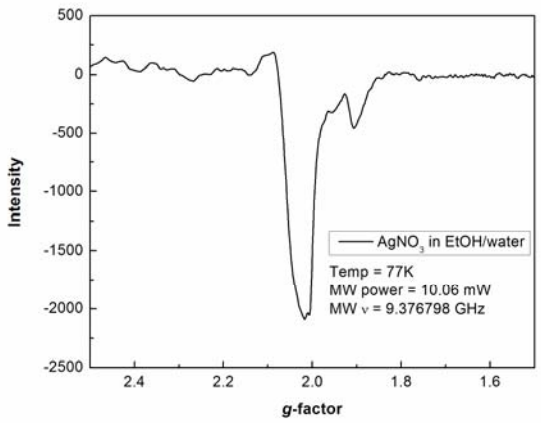

Figure S8. EPR spectrum of a 0.5M $AgNO_3$ solution in 5:1 ethanol/water at 77K shows the presence of at least one paramagnetic species. The poor resolution and low signal to noise suggest that this species is in very low concentration and is probably the result of several different paramagnetic states.

Mass Spectrometry

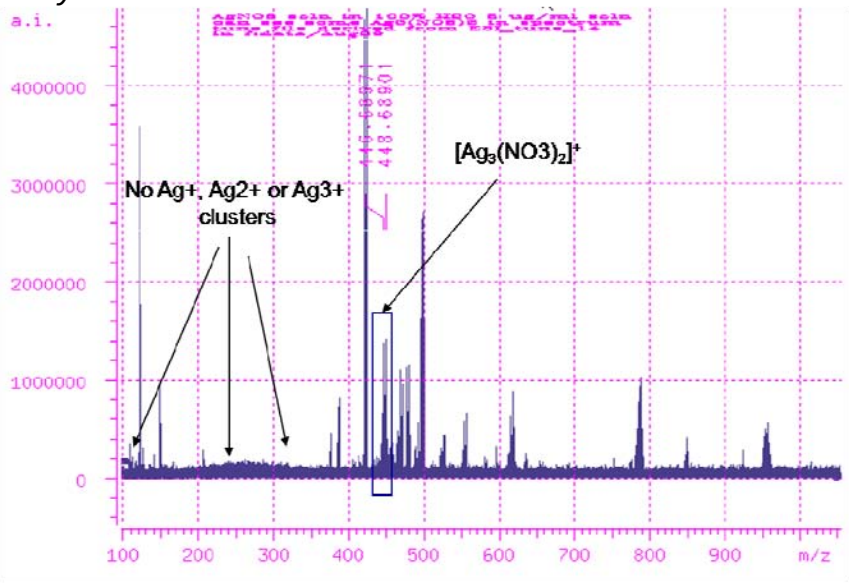

Figure S9. ESI mass spectrum of 5µg/mL $AgNO_3$ prepared by dilution in OmniPure water of 85 mg/mL $AgNO_3$ in 5:1 Ethanol/nanopure water. The spectrum shows the presence of $[Ag_3(NO_3)_2]^+$ is observed at ~446 m/z along with higher order $AgNO_3$ adducts at ~615, 785, and 955 m/z, all separated by 170 D ($AgNO_3$ = 169.7 D.) There are no detectable smaller clusters containing Ag either as Ag^0 or Ag^+. An Ag_3 cluster would show a 1:3:3:1 pattern from 321-327 m/z. The other species below 150 and between ~400-600 m/z are likely polymer or plasticizer impurities leached by the ethanol used in the preparation.

Transmission Electron Microscopy

All MOF samples were imaged using a JEOL 2010F field emission electron microscope operating at 200 kV. The MOF samples were suspended in ethanol and sonicated. A copper TEM grid with lacey carbon support film was then dipped into the solution and allowed to dry. For bright field imaging, a cryogenic TEM stage (Gatan model 636) was used to keep the MOF samples cooled to ~100 K using liquid nitrogen, to help minimize electron beam damage.

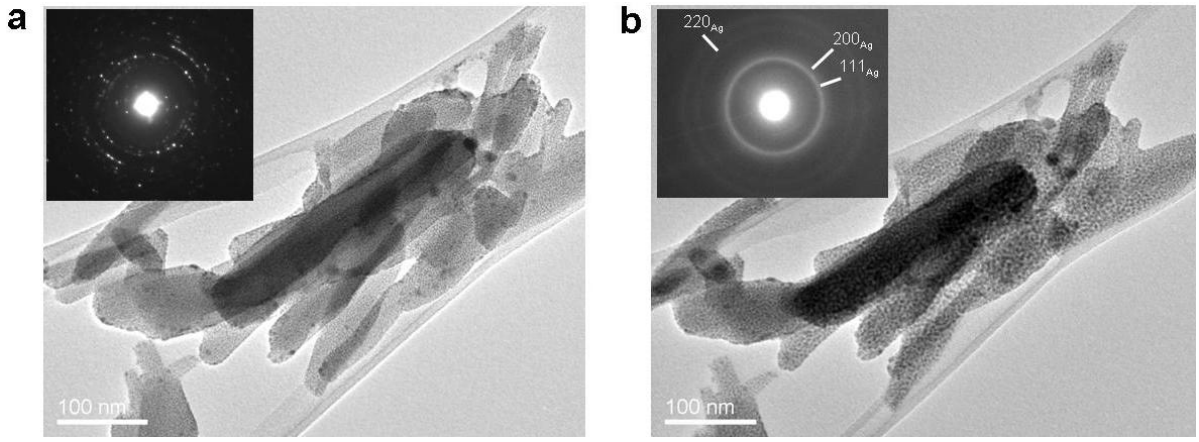

Figure S10. TEM images of Ag@MOF-508 a) before and b) after extended electron beam exposure. The before image shows little change in contrast throughout the bulk of the crystals and the MOF crystal structure is intact as indicated by the inset SAED pattern. After beam exposure the presence of particulate Ag is readily apparent and the MOF has undergone significant beam degredation and no long range order of the crystal remains. The inset SAED pattern shows a *fcc* Ag polycrystalline diffraction pattern and no contribution from the MOF.

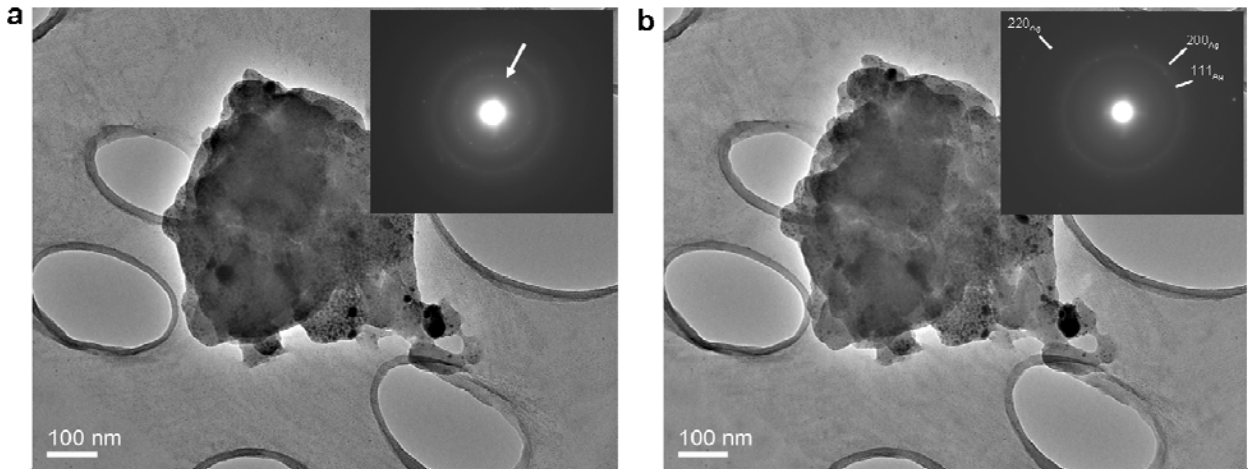

Figure S11. TEM images of Ag@Cu(BTC) a) before and b) after extended electron beam exposure. The dark contrast areas in a) are larger particles of Ag. The arrow in the SAED pattern in the inset indicates diffraction from the HKUST. After extended beam exposure this diffraction has disappeared in as shown in the SAED pattern in the inset in b). The HKUST has undergone significant beam degradation and no long range order of the crystal remains. The inset SAED pattern shows a *fcc* Ag polycrystalline diffraction pattern and no contribution from the HKUST.

Discussion of Movie Files

Ag@MIL-68(In) breakdown.mov: The camera will move to the left over an area of unexposed material, which will begin to quickly degrade. The changing Bragg conditions of the MOF crystal will cause a wave-like dark contrast progression along the lateral direction as it degrades. Ag particles will then coalesce into spherical particles on the 2-5 nm range. The camera will move further to the left over more unexposed regions with the same result.

Ag@MOF-508 breakdown.mov: The camera will move to the left over an area containing several needle-like crystallites unexposed to the electron beam. Under the beam irradiation, the MOF crystals will quickly degrade and shrink, and the Ag will visibly coalesce in to spherical particles.

Ag@MOF-508 breakdown-walkingBragg.mov: After a few seconds, the camera will move down and to the right over an area of material previously unexposed to the electron beam. As the electron beam degrades the MOF crystal, the changing Bragg conditions of the crystal will cause a dark contrast wave-like effect throughout the framework, and again the Ag will coalesce.

Electron Tomography

A JEOL 2010F field emission electron microscope operating at 200 kV with a high-angle annular dark- field (HAADF) detector in scanning TEM (STEM) mode with a camera length of 15 cm at 225 pA beam current. Images of the same area of Ag@MOF-508 were taken every one degree of tilt along a range of ±35°. For the movies labeled "wideangle", a thin tip holder with a theoretical tilt range of ±70° was used to minimize elongation. Practical tilt angles used in this reconstruction are from +70° to -51°. The images were aligned and the tomograph reconstructed; visualization of the reconstruction was then performed.[4, 5] Assuming the set of HAADF images have ~ 1 nm resolution, using the Shannon-Whittaker treatment given in Hoppe, the tomograph

retains ~ 1.8 nm resolution in the vertical direction of the beam direction (Z) and 1 nm in X-Y plane.[6, 7]

Discussion of Movie Files

Tomography-Ag_only.mov: This movie shows the 3D reconstruction of the Ag separated from the MOF-508 matrix by simple mass contrast. The image shows globular particles of the 5-7 nm size range. (Note: the MOF crystallinity has been destroyed by the electron beam and the silver has coalesced.)

Tomography-MOF_only.mov: This movie shows the 3D reconstruction of MOF-508 separated with the Ag removed by simple mass contrast. (Note: the MOF crystallinity has been destroyed by the electron beam and the silver has coalesced.)

Tomography-Combined.mov: This movie combines the two components to show the Ag (blue) embedded throughout the bulk of the MOF (yellow.) (Note: the MOF crystallinity has been destroyed by the electron beam and the silver has coalesced.)

Tomography-Ag_only_lowmag.mov: A zoomed out view of Ag@MOF-508, showing only the Ag only, which though coalesced into large agglomerates from beam damage, still retains the remnants of long-range three dimensional order provided by the MOF during the templating process.

Tomography-Combined_lowmag.mov: A zoomed out view of the combined Ag@MOF-508 showing the Ag clusters well distributed throughout the MOF matrix on a wider range.

Tomography-Ag_only_wideangle.mpg: Full rotation movie of an Ag@MOF-508 crystal examined using the thin-tip holder on a tilt range of -51° to +70°. The resolution of individual Ag clusters is much greater and the elongation is greatly minimized.

Tomography-Ag_only_wideangle_zoom.mpg: Zoomed in version of the previous movie showing again the enhanced resolution.

Tomography-Ag_only_wideangle_zoom_stereo.mpg: Stereo version of the previous movie. Requires the use of red-blue filter glasses to achieve full effect.

1. Chui, S. S. Y.; Lo, S. M. F.; Charmant, J. P. H.; Orpen, A. G.; Williams, I. D. *Science* **1999,** 283, (5405), 1148-1150.
2. Chen, B.; Liang, C.; Yang, J.; Contreras, D. S.; Clancy, Y. L.; Lobkovsky, E. B.; Yaghi, O. M.; Dai, S. *Angew. Chem. Int. Ed.* **2006,** 45, (9), 1390-3.
3. Volkringer, C.; Meddouri, M.; Loiseau, T.; Guillou, N.; Marrot, J.; Férey, G.; Haouas, M.; Taulelle, F.; Audebrand, N.; Latroche, M. *Inorg. Chem.* **2008,** 47, (24), 11892-11901.
4. Harlow, M. L.; Ress, D.; Stoschek, A.; Marshall, R. M.; McMahan, U. J. *Nature* **2001,** 409, (6819), 484.
5. Pettersen, E. F.; Goddard, T. D.; Huang, C. C.; Couch, G. S.; Greenblatt, D. M.; Meng, E. C.; Ferrin, T. E. *J. Computational Chem.* **2004,** 25, (13), 1605-1612.
6. Hoppe, W.; Hegerl, R., Three-dimensional structure determination by electron microscopy (nonperiodic specimens). In *Computer processing of electron microscope images*, Hawkes, P. W., Ed. Springer-Verlag: Berlin, 1978; Vol. 13.
7. Midgley, P. A.; Weyland, M. *Ultramicroscopy* **2003,** 96, (3-4), 431.

[Blank page following section.]

DISTRIBUTION

1	MS0123	D. Chavez, LDRD Office	1011
2	MS0899	Technical Library	9536
2	MS9018	Central Technical Files	8944
1	MS9291	Mark Allendorf	8651
1	MS9404	Rion Causey	8651


Sandia National Laboratories